

# Experimental Study of a Scramjet Nozzle Flow Using the Pressure-Sensitive-Paint Method

C. Hirschen,\* A. Gülhan,† W. H. Beck,‡ and U. Henne§  
DLR, German Aerospace Center, 51147 Cologne, Germany

DOI: 10.2514/1.34626

An experimental study on scramjet nozzle flows was carried out at the DLR, German Aerospace Center. The tests were performed at a freestream Mach number of 7 in the hypersonic wind tunnel H2K in Cologne. The Reynolds number in the tunnel flow was varied to study the performance of the scramjet nozzle at different flight altitudes. The effects of different nozzle pressure ratios were investigated and compared. The static pressure distribution on the single expansion ramp was measured by both the pressure-sensitive-paint method and pressure-system-incorporation pressure transducers. The pressure-sensitive-paint method enables one to gain detailed field information about the pressure distribution on the entire nozzle surface. A pitot rake was used to measure the pitot-pressure distribution in the nozzle wake. The data obtained by the different measurement techniques permitted a characterization of the nozzle flow and gave an insight into the properties of scramjet nozzle flows.

## Nomenclature

$A$	=	area, $m^2$
$M$	=	Mach number
$p$	=	pressure, $N \cdot m^{-2}$
$Re_U$	=	unit Reynolds number, $m^{-1}$
$T$	=	temperature, K
$x$	=	streamwise distance from nozzle entry, mm
$y$	=	spanwise direction from nozzle centerline, mm
$z$	=	height above or below flap, mm
$\alpha$	=	angle of attack, deg
$\gamma$	=	heat-capacity ratio
$\Pi$	=	nozzle pressure ratio, $p_{0,N}/p_\infty$
$\rho$	=	density, $kg \cdot m^{-3}$

## Subscripts

$N$	=	nozzle conditions
stat	=	static
0	=	total conditions
$\infty$	=	wind-tunnel freestream conditions

## I. Introduction

TO SAVE weight and increase the maximum payload of space transportation systems, airbreathing propulsion is an alternative to the existing rocket propulsion systems that carry their oxidant (e.g., liquid oxygen) onboard [1–3]. Aerodynamic stability and generation of sufficient thrust are major problems of a hypersonic vehicle with scramjet propulsion, whereby the nozzle and external

base flow interactions play a large role [4]. Although the interaction of the hypersonic nozzle/afterbody flowfield with a cold plume flow has been extensively studied [5–7], there is still a lack of experimental data. It is therefore necessary to study the aerodynamic phenomena that arise from the interaction between the outer base flow and the hot nozzle flow and to understand their effects on the nozzle performance. This interaction is mainly driven by temperature, viscosity, and heat-capacity-ratio effects.

The dynamic interactions between the aerodynamics of the vehicle and the thrust have also been studied numerically [8,9]. Ebrahimi [10] introduced an efficient design code for scramjet nozzle design. Ishiguro et al. [11] showed the results of a three-dimensional analysis of scramjet nozzle flows that agree well in certain aspects with the experimental results. In [12], the effects on the flow interaction of employing simulant gases instead of air for the scramjet nozzle flow are presented. Experimental studies investigating the interactions between the external flow and internal nozzle flow have been shown to be very complex and are not fully understood as yet [13–15]. In [16], a broad experimental study on the boundary-layer effects in a scramjet nozzle was carried out. These experimental and numerical studies, however, point to the necessity of further research in this field. By applying the pressure-sensitive-paint (PSP) method to hypersonic nozzle flows, the pressure distribution on the entire expansion ramp is obtained and contributes a new and much more detailed data set to existing results. Furthermore, the flowfield in the wake of the single-expansion-ramp nozzle is visualized along different planes by pitot-pressure measurements.

As part of a research project that aims to improve the key technologies for the design of a scramjet propulsion unit [17], it is the goal of the present study to investigate the flow of a scramjet nozzle and to carry out an experimental study of its performance. Mitani et al. [18] performed an experimental study on the performance of a scramjet nozzle in which they compared the experimental data with the results obtained by an inviscid two-dimensional chemical kinetic code. They showed that lift thrust and main thrust are comparable and are very sensitive to the nozzle configuration.

One of the objectives of the present study is to gain information about the nozzle flow of a single-expansion-ramp nozzle and its interaction with the external flow. Therefore, different measurement techniques are applied and the results are compared with each other. The different measurement techniques enable the visualization of different flow aspects such as shock positions, shear-layer position, surface pressure distribution, and exhaust-plume shape. Shock and shear-layer position, as well as the shape of the exhaust plume, were measured and visualized by means of pitot-pressure measurements and schlieren photographs. (The latter, which were already presented in [19], will not be further discussed here.) The surface pressure

Presented as Paper 5088 at the 43rd AIAA/ASME/SAE/ASEE Joint Propulsion Conference and Exhibit, Cincinnati, OH, 8–11 July 2007; received 17 September 2007; revision received 8 February 2008; accepted for publication 20 February 2008. Copyright © 2008 by Christian Hirschen. Published by the American Institute of Aeronautics and Astronautics, Inc., with permission. Copies of this paper may be made for personal or internal use, on condition that the copier pay the \$10.00 per-copy fee to the Copyright Clearance Center, Inc., 222 Rosewood Drive, Danvers, MA 01923; include the code 0748-4658/08 \$10.00 in correspondence with the CCC.

\*Ph.D. Student, Wind Tunnel Department, Institute of Aerodynamics and Flow Technology, Linder Höhe. Student Member AIAA.

†Head, Wind Tunnel Department, Institute of Aerodynamics and Flow Technology, Linder Höhe. Member AIAA.

‡Research Scientist, Institute of Aerodynamics and Flow Technology, Bunsenstr. 10, 37073 Göttingen. Senior Member AIAA.

§Research Scientist, Institute of Aerodynamics and Flow Technology, Bunsenstr. 10, 37073 Göttingen.

distribution is obtained by pressure static measurements (using embedded sensors) and the PSP method. This latter method allows the measurement of the pressure distribution on the entire surface of the model and therefore gives more information than the static pressure measurements. The application of the PSP method in the hypersonic flow regime has already been successfully demonstrated by Hubner et al. [20] and Matsumura et al. [21]. A further goal of this experimental study is to validate the application of the PSP method for use in the hypersonic wind tunnel H2K; this is accomplished by comparing the PSP with the static pressure measurements. The PSP method was used here to obtain pressure distributions over the entire surface of the expansion ramp. Previous experimental studies [22] had shown an anomalous behavior of the static pressure along the centerline of the expansion ramp. Rather than the expected monotonic decrease in the static pressure distribution along the centerline due to the acceleration of the flow, it was found to vary (increase and decrease several times) in the flow direction. This wavy behavior was very odd and had to be further investigated to be fully understood.

These experiments were performed at a freestream Mach number  $M_\infty = 7$  and Reynolds numbers of  $Re_U = 4 \times 10^6$  and  $8 \times 10^6$ , corresponding to flight altitudes of 30 and 25 km, respectively. According to former experimental studies, the nozzle pressure ratio  $\Pi$  and the freestream Reynolds number  $Re$  are the main parameters affecting the nozzle flow behavior [22]. Therefore,  $\Pi$  is varied to study its influence on the shock and shear-layer positions, the exhaust-plume shape, the pressure distributions, and the gross thrust. The experimental results obtained by the pitot-pressure measurements and the PSP method are compared with gain-complementary information about the flow properties of this scramjet nozzle.

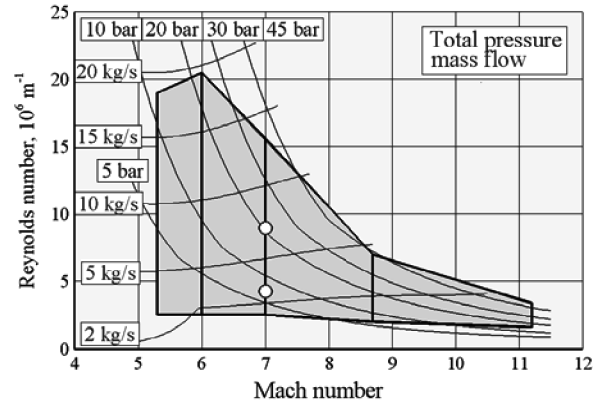
## II. Experimental Methods

### A. Wind Tunnel and Test Conditions

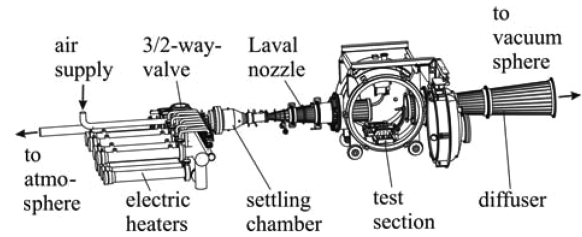
The experiments were carried out in the H2K hypersonic wind-tunnel facility of the DLR, German Aerospace Center in Cologne. This facility is a blowdown wind tunnel with test durations of up to 30 s, depending on the flow conditions. The facility is equipped with five contoured nozzles with varying throat diameters and a constant exit diameter of 600 mm, leading to flow Mach numbers of  $M_\infty = 5.3, 6, 7, 8.7,$  and  $11.2$ . For these experiments, the Mach-7 nozzle was used. Dried air passed from a pressure reservoir with a maximum pressure of 4.5 MPa through electrical heaters with a heating power of 5 MW, thereby heating the air to temperatures of up to 1000 K; this avoids later potential condensation effects in the nozzle expansion. The operational range of the H2K wind tunnel can be seen in Fig. 1a, in which the performance map with respect to the Mach number and unit Reynolds number  $Re_U$  is depicted, with total pressure  $p_0$  and mass flow rate  $\dot{m}$  as parameters. The thick black vertical lines pertain to the available wind-tunnel nozzles. The unit Reynolds number is given by the proper choice of the total pressure  $p_0$  and  $T_0$  of the flow. A schematic sketch of the hypersonic wind-tunnel facility is shown in Fig. 1b. The wind-tunnel flow conditions for these tests with the nozzle model are summarized in Table 1; the accuracy of measurement is as follows:  $\Delta M/M = 0.50\%$ ,  $\Delta T_0/T_0 = 0.75\%$ , and  $\Delta p_0/p_0 = 0.02\%$ .

### B. Model and Experimental Setup

Experiments with a single-expansion-ramp nozzle equipped with a generic forebody were carried out (see Fig. 2). This forebody was designed to fit onto the existing single-expansion-ramp nozzle (Fig. 2b) and to supply this nozzle with its own (exhaust) gas flow; in these experiments, this gas was not heated. During these tests, the model and tunnel axes were aligned in parallel. The exhaust gas was supplied to the nozzle plenum by a pipe, which was mounted on the side of the forebody at one end and connected to a tube at the other end. Through this connecting tube, the different gases, which are stored in external separate reservoirs near the wind tunnel, were injected into the model plenum. To provide a uniform flow, a honeycomb followed by a contoured 2-D Laval nozzle (Fig. 2b) were



a) Performance map



b) Schematic sketch

Fig. 1 Hypersonic wind-tunnel facility H2K.

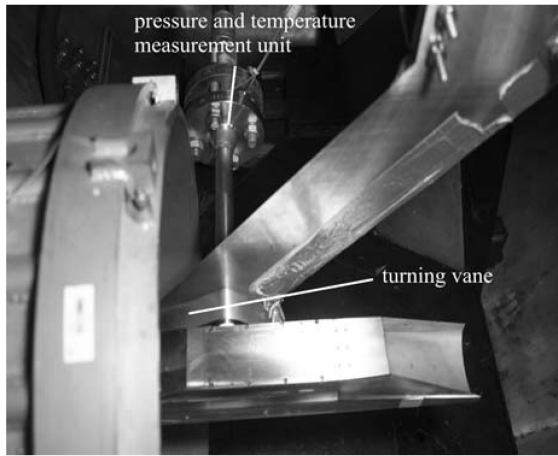
installed inside the forebody. The Laval nozzle was necessary to provide supersonic flow and to simulate the Mach number at the combustor exit, which was  $M = 2$  for these experiments. The entrance to the single-expansion-ramp nozzle has a cross-sectional area of 19-mm height by 60-mm width.

The model is a 3-D single-expansion-ramp nozzle (see Fig. 3) with a total length of 214 mm and a total height of 101 mm. This nozzle was originally designed in the framework of the Japhar program [23]. The nozzle is equipped with 51 pressure taps (orifices) in total. There are four on the cowl, three on the side, and 44 on the ramp, these being placed along three different lines in the flow direction. Thirty are on the centerline, eight are displaced 15 mm to the right side, and six are displaced 30 mm to the left side of the centerline (see Fig. 3), as seen when looking down the nozzle in the flow direction. In Fig. 3b, the positions of the pressure orifices are marked by the black dots.

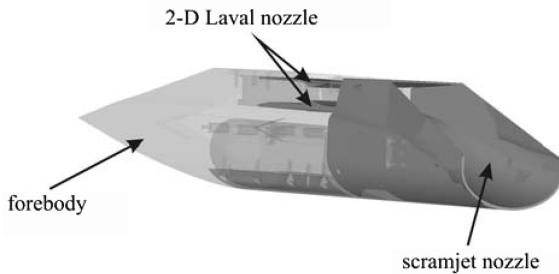
Figure 4 shows two pictures of the nozzle model installed in the wind-tunnel section. It can be seen that the model is held by a strut that is mounted to the side of the model and connected by an adapter to the model to attain a certain separation between the strut and the model. This separation prevents the shock originating from the strut leading edge from perturbing the nozzle flowfield. The strut is mounted to a model holder that can be pitched to change the angle of attack and angle of yaw of the model. During a test run, the angle of attack can be varied continuously, whereas only one position for the angle of yaw can be set. The wind-tunnel flow is started as soon as the required pressure in the jet plenum has been achieved. The coordinate system used in this paper is shown in Fig. 4 (bottom), the origin being marked with 0.

Table 1 Wind-tunnel flow conditions

Freestream Mach number $M_\infty$	7	7
Freestream pressure $p_\infty$ , Pa	260	515
Freestream temperature $T_\infty$ , K	60	60
Freestream density $\rho_\infty$ , kg/m <sup>3</sup>	0.015	0.029
Total temperature $T_0$ , K	650	650
Total pressure $p_0$ , Pa	$10 \times 10^5$	$21 \times 10^5$
Unit Reynolds number $Re_U$ , 1/m	$4 \times 10^6$	$8 \times 10^6$

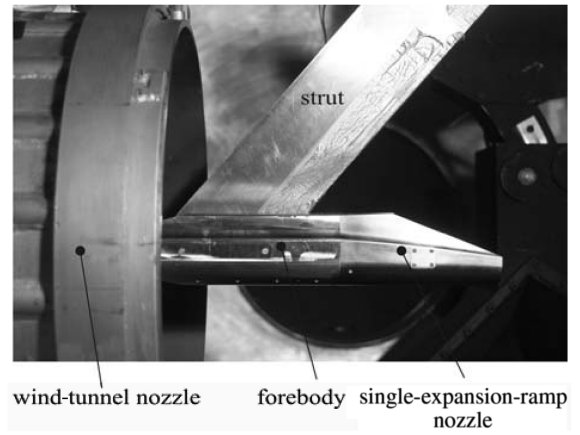


a) Model in wind tunnel



b) 3-D sketch of forebody and nozzle

Fig. 2 Forebody and nozzle.



wind-tunnel nozzle forebody single-expansion-ramp nozzle

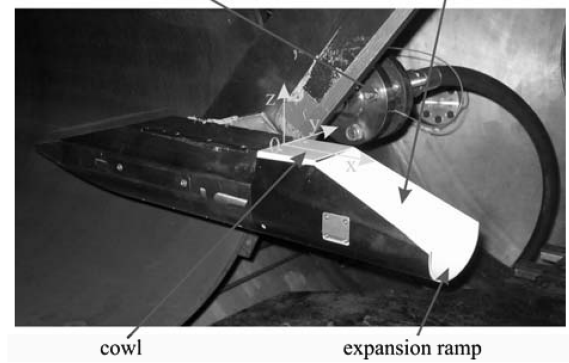
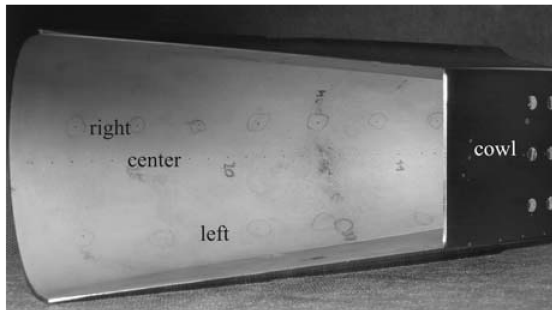
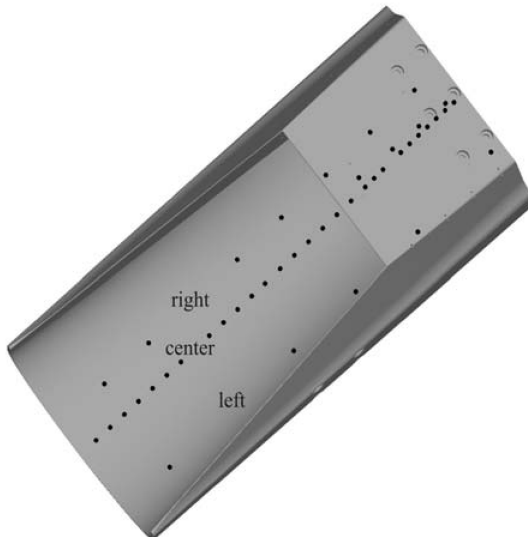


Fig. 4 Side view of the nozzle model connected to a forebody.



a) Photo of nozzle



b) 3-D sketch of nozzle

Fig. 3 Pressure orifices of the three-dimensional single-expansion-ramp nozzle.

### C. Measurement Techniques

Because the density and thus the density gradients in H<sub>2</sub>K are low, a coincident schlieren optical setup is used to visualize the flowfield. With this technique, the light beam traverses the test section twice, which leads to a higher sensitivity, but also to a slightly lower resolution. To study unsteady flow phenomena in the nozzle region, a high-speed schlieren camera had been used in a previous experimental study. Based on the results of these experiments, which showed no resolvable unsteady effects, an analog camera with a higher resolution was used in this experimental study [19]. (The schlieren results are not further discussed here.)

During the experiments, the jet total pressure  $p_{0,N}$  and total temperature  $T_{0,N}$  are measured with a pitot tube and a thermocouple in the plenum chamber upstream of the honeycomb. The static pressures on the single-expansion-ramp nozzle are measured with a pressure-system-incorporation (PSI) module with the range of 15 psi (approximately 105 kPa). The forebody was designed to fully accommodate the PSI module, so that the pressure tubes connecting the pressure taps (orifices with diameter 0.5 mm) and the module could be kept as short as possible.

### D. Pitot-Pressure Measurements

To obtain a pressure distribution of the flowfield, pitot-pressure measurements were carried out. The pitot rake had 14 pitot probes placed 6 mm apart, leading to a total pitot rake span of 79 mm. In applying pitot-pressure measurements in supersonic and hypersonic flow regimes, a normal shock wave occurs in front of the pitot tube. Therefore, the pitot pressure  $p_{\text{pitot}}$  behind the normal shock wave, and not the total pressure  $p_0$ , is measured. With the assumption that the total pressure  $p_0$  is constant within the isentropic flowfield of the nozzle, the Mach number distribution can be iteratively calculated by solving Eq. (1):

$$\frac{p_{\text{pitot}}}{p_{0,N}} = \left( \frac{\gamma - 1}{\gamma + 1} + \frac{2}{(\gamma + 1) \cdot M^2} \right)^\gamma \cdot \left( \frac{2\gamma}{\gamma + 1} \cdot M^2 - \frac{\gamma - 1}{\gamma + 1} \right)^{-\frac{1}{\gamma - 1}} \quad (1)$$

With the Mach number distribution and the total pressure  $p_0$ , the static pressure distribution in the flowfield can now be calculated by using Eq. (2):

$$P_{\text{stat}} = P_{\text{pitot}} \left/ \left[ \left( \frac{\gamma + 1}{2} \right) \cdot M^2 \cdot \left\{ \left[ \left( \frac{\gamma + 1}{2} \right) \cdot M^2 \right] / \left[ \frac{2\gamma}{\gamma + 1} \cdot M^2 - \frac{\gamma - 1}{\gamma + 1} \right] \right\}^{\frac{1}{\gamma - 1}} \right] \right. \quad (2)$$

To measure the pitot-pressure distribution in the entire flowfield, the pitot rake is displaced in the horizontal  $x$  and vertical  $z$  directions. Figure 5 shows the displacement unit. The pitot rake is mounted to a rod that is moved in a vertical direction by a linear motor, and a potentiometer is used to measure its position. The entire unit of potentiometer, rod, and pitot rake can be moved in the  $x$  (flow) direction. The measurement of the pitot pressure at different  $z$  and  $x$  positions enables a mapping of the flow over and downstream of the nozzle. The achieved spatial resolution of this process depends on the adopted step sizes in the  $z$  and  $x$  directions; here,  $\Delta z = 2$  mm and  $\Delta x = 30$  mm were used. Hence, for each  $x$  position, a grid of points in the  $y$ - $z$  plane is measured; with  $\Delta y = 6$  mm and  $\Delta z = 2$  mm as grid spacing, the representation as a continuous flowfield can be obtained by interpolating between the discrete points.

The pitot tubes are also connected to a PSI module with the same operating range of 15 psi, which records and then digitizes the pressure values in a scanner interface, from which they are sent to a computer.

### E. PSP Method

The PSP measurement technique as used here is based on the photochemical deactivation by oxygen molecules of excited (paint) molecules called luminophores. When luminophores absorb light, they are excited to a higher energy state, from which they can become deexcited (relax) via radiative and nonradiative processes [the latter can involve collisions with other molecules (quenchers) and internal relaxation]. The interaction (collisions) of these excited luminophores with oxygen molecules leads to greater nonradiative relaxation, which in turn leads to a decrease in the emitted fluorescence; the intensity of this emitted fluorescence is therefore related to the oxygen density, which, under certain assumptions, can then be expressed as the total local pressure [24].

The paint sensor used here, called the DLR02 formulation, consists of two polymeric layers that are applied consecutively to the model surface. They are the white screen layer and the active layer with its luminophores. The screen layer is composed of a special white paint that creates an optical uniformity on the model surface, independently of the model material; it also increases the reflection of light. The active layer consists mainly of three components: 1) a polymer layer that is highly permeable to oxygen (binder), 2) a pressure-sensitive luminescent luminophore dispersed within the polymer, and 3) intensity-sensitive luminophores (which are sensitive only to illumination intensity and are insensitive to pressure and temperature) for intensity correction of the nonhomogeneous distribution of illumination.

A calibration of the optical pressure system is necessary for reconstructing a quantitative pressure image from the initial raw images captured by the cameras on the surface of the model. This was

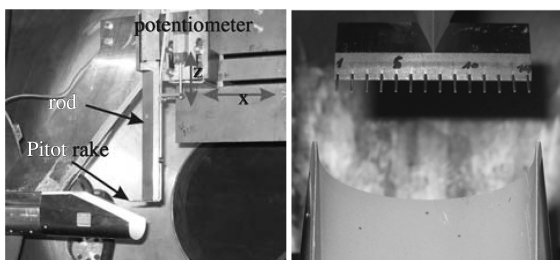


Fig. 5 Pitot rake displacement unit (left) and pitot rake (right).

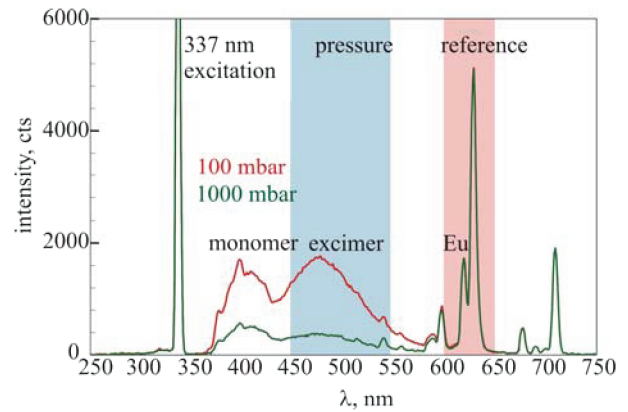


Fig. 6 Emission spectra of the binary pyrene-based paint DLR02.

done in two different ways. In the first, a test specimen is coated at the same time and using the same method as for the model and is subsequently subjected to known pressures and temperatures in an external calibration chamber. For the other method, the entire model was calibrated in H2K itself, in which it was possible to attain and maintain various static (wind-off) pressures in the test section. In the external calibration chamber, the pressure and the temperature can be varied and, consequently, the described temperature-dependent calibration constants can be determined and related to pressure reconstruction. The temperature of the model surface necessary for correcting the pressure computations was measured during the experiment using a Thermacam 3000 (FLIR Systems) IR camera.

The DLR02 formulation was developed in cooperation with the Organic Chemistry Institutes of the Universities of Göttingen and Hohenheim. It contains a pyrene derivative as the pressure-sensitive dye and a Europium complex as the reference dye. The two components of the paint absorb ultraviolet radiation and emit at different higher wavelengths; Fig. 6 shows the emission spectrum of the paint DLR02 when excited at 337 nm for two different pressures: 100 and 1000 mbar (approximately 10 and approximately 100 kPa).

For the luminophore excitation, a flash lamp operating at 20 Hz was used. The light was coupled into four fiber optic cables (liquid-filled) of 10-m length, which were bundled together and brought via a tube mounted internally in the test section to a distance of about 1 m above the test model (see Fig. 7). A DUG-11 filter was placed at the end of the fiber bundle to remove all but the exciting wavelength light. Two cooled PCO CCD cameras with 12-bit resolution and exposure times of 1.7 s were used for image acquisition; hence, the fluorescence arising from about 34 flash-lamp pulses was cumulatively stored on the CCD chips, leading to an averaging of the pressure levels over this time window. By using filters in front of the cameras, one camera was able to capture the pressure-sensitive (blue: 450–550-nm) signal, the other captured the reference pressure-insensitive (red: 600–650 nm) signal.

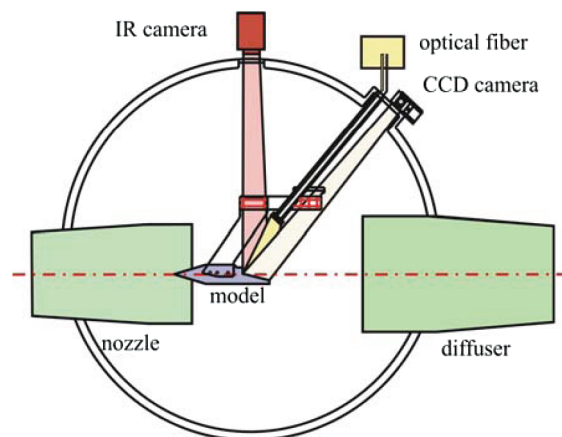


Fig. 7 Setup for PSP.

An automated acquisition system (here, a PC) was used to couple the DLR-PSP and the H2K data acquisition systems. The PSP-PC transferred the data to a Sun workstation running the DLR software ToPas (three-dimensional optical pressure analysis system), which was used to store and process the data and to enable a first quick-look interpretation of the pressure results right after each test run.

### F. Estimation of Uncertainties in the PSP Measurements

The total uncertainty (error) in the PSP results consists of the sum of its two components: bias uncertainty (systematic errors) and precision uncertainty (repeatability).

#### 1. Bias Uncertainty

A systematic discussion of elemental error sources contributing to bias uncertainty has been given by Liu et al [25]. In summary, these are listed next, with comments pertaining to the measurements in this work:

1) With large CCD signals (shot noise, dark current, amplifier noise, quantization noise), this effectively reduces to just the shot noise with its well-known  $N^{1/2}$  dependence.

2) The model is not movable and is rigidly mounted; the error source is negligible.

3) The paint used here also has a weak temperature dependence of 1.4 mbar/K over the temperature range of 273–293 K (with a higher dependence of 2.8 mbar/K at 263 K), which is approximately constant over the experimental pressure range of 30–120 mbar. As already described, this dependence is measured in a separate calibration chamber in which both temperature and pressure can be varied over ranges encompassing the expected tunnel values. Wind-on and wind-off IR-thermography images were also captured, giving the model ramp-surface temperatures during the experiment. A pixel-by-pixel correction of the PSP data using this temperature data is, in principle, possible, but was not performed here. An average surface temperature was adopted, and with the help of the known temperature dependency (1.4 mbar/K; see the preceding) and a parametric processing of the PSP data using temperature as the parameter, the uncertainty arising from this approach could be estimated: a  $\pm 2$ -K temperature variation on the surface leads to a pressure inaccuracy of  $\pm 2.8$  mbar.

4) PSP calibration was carried out in the aforementioned calibration chamber and, as a check, in situ in the tunnel, in which pressure (but not temperature) in the test section could be varied.

5) Spectral-variability/filter-leakage contribution is small; the large distance from camera to model (over 1 m) and the model dimensions on the order of 20 cm lead to a viewing angle of only about 10 deg, resulting in a low-filter spectral shift.

6) The available ToPas software uses several (up to 10) markers placed at strategic points on the test model to perform pressure mapping (mapping 2-D images to the grid of a 3-D model); accuracy is better than 1 pixel.

7) Self-illumination (because the ramp surface is quite flat), paint intrusiveness (measurements with and without paint showed the same results with the PSI sensors), and time response (because only average pressures were measured over the 1.7-s viewing time, and because tunnel pressure fluctuations had a period  $\ll 2$  s, the paint time response does not lead to a false measurement) are negligible.

#### 2. Precision Uncertainty

Five separate image pairs were captured in the run of about 20 s; they showed no variation (the tunnel conditions over this time were also measured to be constant). Furthermore, two runs were carried out at nominally identical conditions, with comparable PSP results (due to the nature of tunnel operation, however, the run conditions were not exactly identical).

Using an approach discussed by Sajben [26], the total uncertainty from all sources was estimated as the square root of the summed squares of the individual errors. By far, the largest contribution comes from the (known) variation in temperature over the surface, which is  $\pm 2$  K (this corresponds to an error in adopted temperature

of  $\pm 0.71\%$  for the measured temperature range). The total error for PSP is about 5%.

## III. Experimental Results and Discussion

### A. PSP Results

Figure 8 shows the normalized static pressure distribution obtained by the PSP method for a freestream Reynolds number of  $Re_U = 8 \times 10^6$  and a nozzle pressure ratio of  $\Pi = 500$ ; also shown are the positions of the pressure orifices on the left, center, and right lines (as described in Sec. II.B). Figures 9a–9c show the results of the PSP measurements along these lines compared with the PSI measurements. For the data obtained with the PSI transducers, the error is 0.15% of the full-scale pressure range of the used PSI module, leading to a measurement uncertainty of 1.55 mbar. Therefore, the error bars for the PSI measurement are of the size of, or smaller than, the symbols representing their values in the figures. Representative PSP error bars are shown in Fig. 9a. All pressures are plotted normalized to the total nozzle pressure  $p_{0,N}$ .

As already stated, the PSP method was implemented here to help explain the wavy behavior or to at least corroborate the previous pressure-sensor measurements. Two-dimensional CFD simulations had already shown that this measured wavy behavior could not be due to any geometrical flaws in the scramjet nozzle design, but rather to the actual behavior of the nozzle flow itself [19,22]. As can be seen

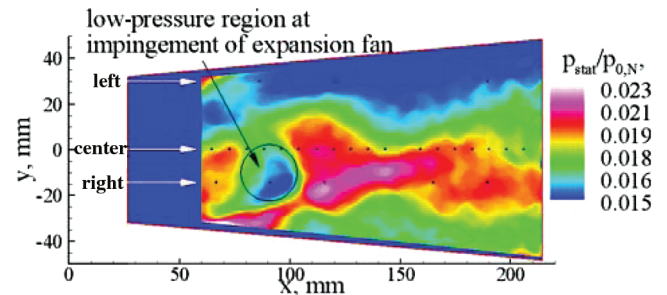


Fig. 8 PSP measurement results for  $Re_U = 8 \times 10^6$  and  $\Pi = 500$ .

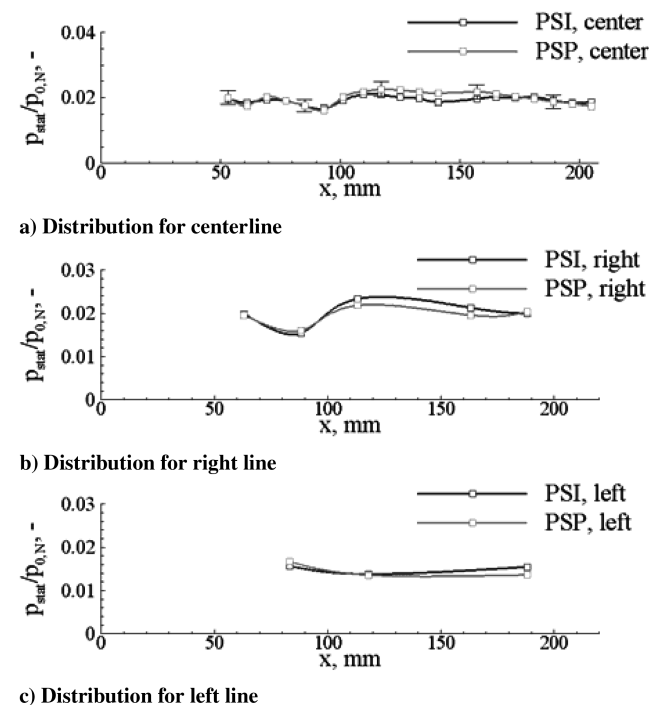


Fig. 9 Comparison between PSI and PSP pressure measurements for  $Re_U = 8 \times 10^6$  and  $\Pi = 500$ .

in Fig. 9a for the centerline, the results of the PSI and PSP measurements show very good agreement at lower and higher values of  $x$ , whereas in the central region, there is a systematic shift between the pressure values that is not completely understood yet. The good agreement is also valid for the static pressure measurements along the left and right sensor lines on the expansion ramp (Figs. 9b and 9c).

The PSP measurements also show the (spatial) wavy behavior of the static pressure distribution along the centerline. The reason for this would seem to be the geometrical shape of the nozzle, which causes an early separation of the exhaust plume and after this separation a rise in the static pressure, this rise being an almost isentropic compression due to the changing slope of the expansion ramp. Because of the continuing acceleration the static pressure decreases again causing the wavy behavior in the pressure distribution. The PSP measurements also revealed that the flow of the scramjet nozzle is asymmetric. This is almost certainly due to the one-sided injection of the gas into the side of the forebody (Fig. 10). The flow obviously does not equilibrate over the entire volume of the settling chamber inside the model so that the flowfield itself becomes asymmetric, reflecting the asymmetric injection. This is potentially a further cause for (or at least an exacerbation of) the wavy behavior of the static pressure distribution seen along the centerline. In the region to the right of the centerline (see Fig. 8) it can be seen that a high-pressure region extends from the lower nozzle side wall all the way up to the centerline. This high-pressure region is situated in which the flow accelerates due to the expansion in the  $x$ - $y$  direction. There is apparently, due to the asymmetric flow, more mass fluid in the part below the centerline; hence the pressure level is higher than in the part above the centerline. The knowledge gained on this asymmetrical flow behavior will be used for the construction of new nozzle models in which the fluid is to be brought symmetrically into the settling chamber to avoid or at least mitigate these phenomena.

## B. IR-Thermography Results

Because the fluorescent intensity of the paint in the PSP method depends not only on the pressure but also on the temperature on the investigated surface, the temperature distribution was measured by an IR camera. Figures 11a–11c show typical results of the temperature measurements, Fig. 11a was taken at the beginning, Fig. 11b was taken in the middle, and Fig. 11c was taken at the end of the test run-time window (here about 17 s). It can be seen that the surface of the expansion ramp is fairly cold at the beginning of the test run, because the accommodation of the surface to the gas flow temperature takes some time. After the wind tunnel has been started and the external flow has been established, the temperature of the surface of the expansion ramp increases. The temperature distribution on the surface is influenced by two competing phenomena: a temperature decrease due to the expansion of the nozzle flow and a temperature increase due to heat conduction caused by the hot external flow. The highest temperatures are obtained at the end (downstream side) of the expansion ramp (right side in Fig. 11), in which the wall thickness is very thin and the heat conduction into the structure is weak. The upstream part of the nozzle has a thicker wall (i.e., higher thermal mass). Therefore, the surface temperature change in this area is small. Because of the high heat conductivity of the model wall, the heat conducts from the hot downstream part to the cooler upstream part of the expansion ramp.

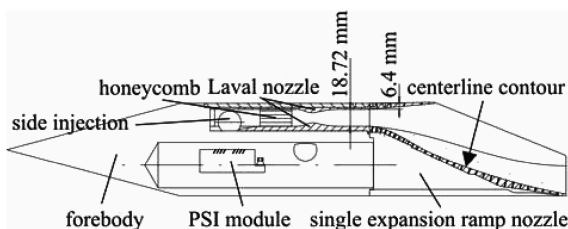
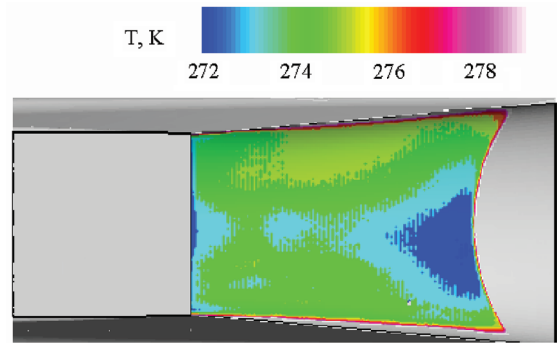
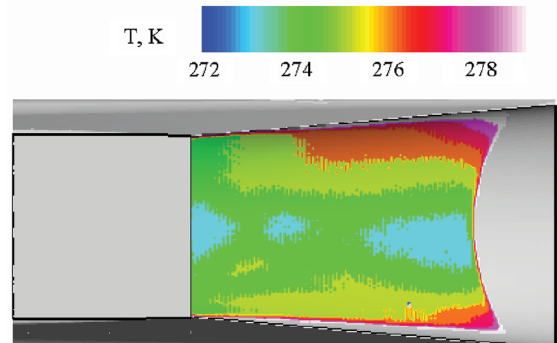


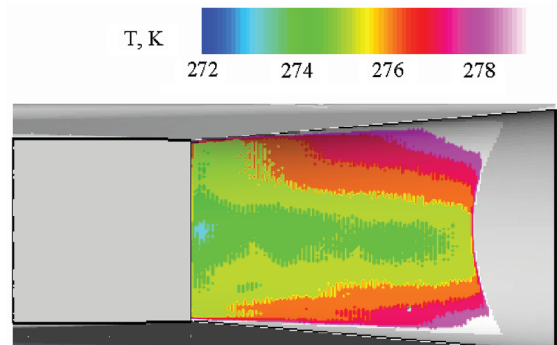
Fig. 10 Sketch of inner components of the model.



a) Distribution at beginning of test run



b) Distribution in the middle of test run



c) Distribution at the end of test run

Fig. 11 Temperature distribution during test run obtained by IR thermography.

## C. Influence of $Re_U$ and $\Pi$

Figures 12a–12c show the influence of the freestream Reynolds number  $Re_U$  and the nozzle pressure ratio  $\Pi$  on the static pressure distribution on the expansion ramp. The Reynolds number is varied between  $Re_U = 4$  and 8 million and the nozzle pressure ratio is between  $\Pi = 500$  and 1000. By comparing Figs. 12a and 12b, the influence of the nozzle pressure ratio can be clearly seen from the different patterns of the static pressure distribution. Again, the nozzle flow is not symmetric relative to the centerline. Assuming that the low-pressure region in the upper part of the expansion ramp is a sign for a very low mass flow rate, a symmetry line can be drawn, as shown in Fig. 12b. This line is seen to be shifted closer to the centerline for  $\Pi = 1000$  and turned toward the lower part of the expansion ramp. From this, one can infer that the nozzle flow does not stream evenly over the entire width of the ramp, but rather is inclined from the upper left corner to the lower right corner of the nozzle in Figs. 12a–12c. Because of its inclination to the ramp axis, the flow impinges onto the side wall at a certain angle, and it is postulated that this leads to the formation of a shock, which extends from the wall in a general downstream direction (Fig. 12a). The pressure distribution shows a sharp pressure rise followed by a rapid pressure decrease. This behavior is not necessarily due to just the shock, but can be amplified by overlying expansion effects. In

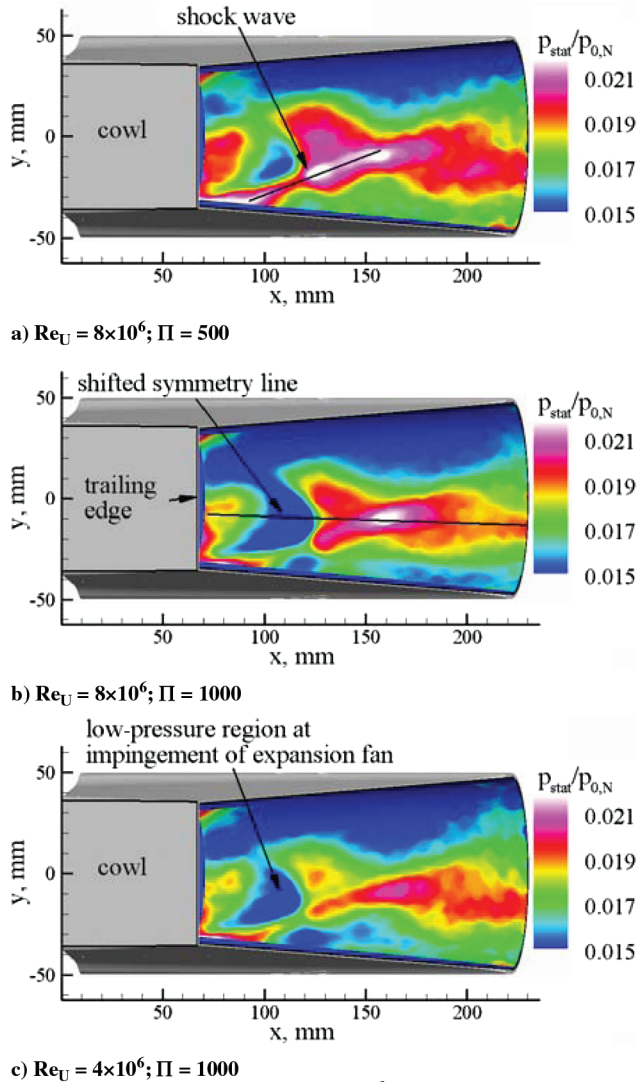


Fig. 12 Influence of freestream Reynolds number  $Re_U$  and nozzle pressure ratio  $\Pi$  on the pressure distribution of the expansion ramp.

Fig. 12b, it can be seen that the pressure rise due to this shock is smaller than in Fig. 12a. Furthermore, quite remarkable in this figure is the large low-pressure region directly upstream of the high-pressure region; it is probably caused by the strong expansion that occurs at the trailing edge of the cowl. At this point, the nozzle flow expands because of the high-pressure difference between internal and external flow. The expansion waves originating from the trailing edge of the cowl impinge on the expansion ramp and create this low-pressure region. In the case of larger  $\Pi$  (Fig. 12b), the pressure difference between internal and external flow is also higher; hence, the expansion is stronger, leading to a larger expansion fan and therefore a larger low-pressure region on the expansion ramp, compared with the result for lower  $\Pi$  (Fig. 12a). Unfortunately, the acquired IR images do not allow the detection of these flow structures, because the heat conductivity of the material is too high and the effects of the shock heating are probably weak. Unfortunately, schlieren results are not available here, because the side walls of the ramp do not allow optical access to the region of interest.

Comparing Fig. 12c with Figs. 12a and 12b, it can be seen that the parameter with the main influence on the nozzle flow is the nozzle pressure ratio  $\Pi$ . For the same  $\Pi$  but differing  $Re_U$  (Figs. 12b and 12c), the flow pattern is very similar, but for the different  $\Pi$ , it differs distinctly. Although the total nozzle pressure is the same in Figs. 12a and 12c, the flow pattern is different, due to the fact that the static pressure of the external flow is different as well. In this case, the

higher  $\Pi$ , as in Fig. 12c, causes a stronger expansion at the trailing edge of the cowl, leading to the similar flow pattern of Fig. 12b, in which the  $\Pi$  is the same. Here, one can also recognize the same structures: the low-pressure region on the upper part of the ramp, in which apparently only very little flow is to be found, the flow pattern created by the expansion fan, and the shock reflected from the side wall. These interactions must clearly influence the thrust and the thrust vector in a deleterious way. The interaction between the shock and the expansion waves, as well as their reflection from the expansion ramp, leads to a complex flowfield with a considerably asymmetric pressure field.

The application of PSP is a useful way of visualizing the pressure distribution on the entire surface of this scramjet nozzle. In the present case, it revealed the asymmetry of the nozzle flow and the complex flow phenomena created by the interaction between the internal and external flow. It helped in the detection and understanding of the flow phenomena in a better way than pressure measurements using only the PSI sensors could provide. The good agreement on the whole with the PSI pressure measurements showed that a qualitatively and quantitatively correct pressure distribution for the scramjet nozzle could be obtained. PSP clearly reveals more information about the flowfield than local PSI pressure measurements and allows a better assessment of the nozzle flow. For complicated model geometries, the thrust can be calculated more easily and accurately by the pressure-sensitive-paint method than by local PSI pressure measurements [27].

#### D. Pitot-Pressure Results

In this present work, the influence of varying  $Re_U$  and  $\Pi$  on the nozzle flow have also been measured with the help of pitot-pressure measurements. Figures 13a–13d show the results of the pitot-pressure measurements at the same value of  $Re_U = 8 \times 10^6$  but at two different values of  $\Pi = 250$  and 500 and at two different  $x$  positions of the pitot rake ( $x = 244$  and 274 mm). Comparing the results at the same position at  $x = 244$  mm, which corresponds to 30 mm downstream of the nozzle, both similarities and differences are evident. The high-pressure level around  $y = 0$  mm and  $z = -85$  mm is very similar in both cases. However, in the upper part of the nozzle flow ( $z > -60$  mm), not only the values for the pressure ratio  $p_{\text{pitot}}/p_{0,N}$  differ, but so does the topology of the flowfield. The separation of the two low-pressure regions (for example, across the line at  $z > -40$  mm) is greater for  $\Pi = 500$  than for  $\Pi = 250$  (Figs. 13c and 13d), due to the stronger expansion of the flow for  $\Pi = 500$ . A lower pressure value means that the Mach number is higher in this region. The high Mach number is caused by three-dimensional effects (expansion also occurs in the  $y$  direction) of this scramjet nozzle. The fact that the low-pressure and high-Mach-number region is further apart in Fig. 13b shows that the exhaust plume is wider in this case. In the case of  $\Pi = 250$ , the exhaust plume is more strongly influenced by the external flow than for  $\Pi = 500$ . Another possible contributor to the differences seen in this region could be the asymmetry of the nozzle flow, which was discussed in more detail before and could be more clearly seen when considering the results of the PSP measurements.

The results in the region below the nozzle ramp (i.e., at  $z < -101$  mm) differ as well. One reason for this is that the measured pressure is related to the total pressure  $p_{0,N}$ , and in the case of  $\Pi = 500$ , this pressure is twice as high as for  $\Pi = 250$ . If the pressure of the external flow is related to the total pressure of the nozzle, the pressure ratio  $p_{\text{pitot}}/p_{0,N}$  is obviously half as high for  $\Pi = 500$  as for  $\Pi = 250$ , because the freestream Reynolds number is the same. But the similarities in the pressure coefficient distribution show that the positions of the shear layer and of the internal and external shocks differ only slightly. This is again due to the different strengths of the expansion at the end of the expansion ramp, which depend on  $\Pi$ . The expansion at the end of the expansion ramp and the gross thrust are strongly dependent on  $\Pi$ ; the higher its value, the stronger the expansion at the end of the expansion ramp.

The pressure ratio  $p_{\text{pitot}}/p_{0,N}$  distribution 60 mm downstream of the nozzle (at  $x = 274$  mm) for  $\Pi = 250$  and 500 are shown in

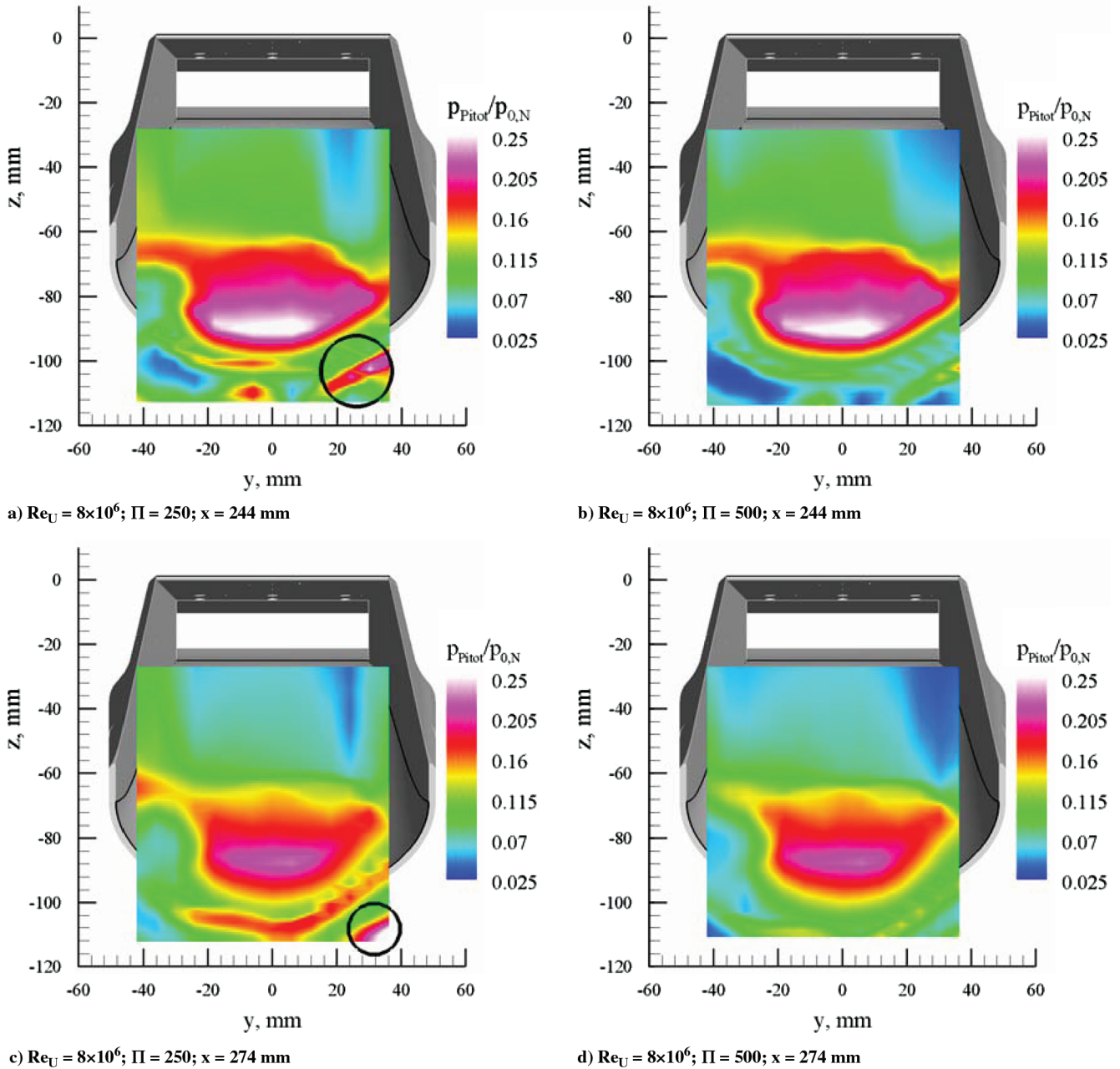
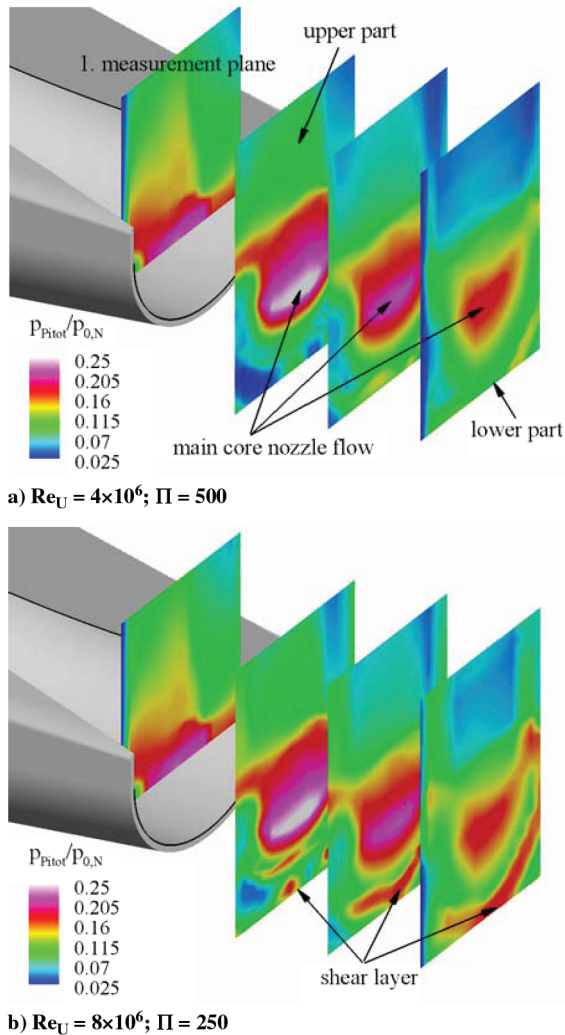


Fig. 13 Pitot-pressure measurements at  $Re_U = 8 \times 10^6$  for  $\Pi = 250$  and  $500$  at two different planes downstream of the nozzle.

Figs. 13c and 13d. The values in the high-pressure region (seen in the lower part of the flowfield) are lower than at  $x = 244$  mm, whereas the values of the low-pressure region in the upper part have also decreased. Now the differences in the upper part can be clearly seen; this is due to the exhaust plume for  $\Pi = 500$  being wider in the  $y$  direction than for  $\Pi = 250$ . The regions of high pressure (red regions) are a sign that the exhaust plume separates too early from the expansion ramp of the nozzle. One can infer from this that the nozzle design is not optimized for these conditions, because the exhaust plume should cover the entire expansion ramp of the nozzle evenly. Considering the three-dimensional geometry of this nozzle, the pressure values should be smaller in the lower part than in the upper part of the  $y$ - $z$  plane, due to the acceleration in the  $x$ - $y$  plane. Another reason for this unexpected behavior could be due to the interaction between the shock and expansion wave discussed in the preceding PSP section. Looking at the flow below the high-pressure region, it can be seen that the shear layer and internal and external shock move downward. This can clearly be seen with the small red region in the lower right corner in Fig. 13c; Figs. 13a and 13c show that this red region (inside the black circle) has moved downward (in the  $z$

direction). Again, slight differences in the positions of the shear layer and shocks occur for the two different nozzle pressure ratios.

Figures 14a and 14b show the results of the pitot-pressure measurements at all four planes in the  $x$  direction and for two different freestream Reynolds numbers. This helps to visualize the flowfield in the wake of the nozzle and to gain more information about the interaction between the internal and external flow. The pressure distribution at all four planes reveals how the flow develops in the wake and how it is influenced by the external flow. Considering the first measurement plane (seen at the very left in Figs. 14a and 14b, it being positioned before the end of the expansion ramp), the results hardly differ between the two conditions in Figs. 14a and 14b. In this region, the nozzle flow is not yet influenced by the external flow. At the next plane further downstream of the nozzle, the first differences become apparent in the upper and lower parts of the plane. The different static pressures of the external flow influence the expansion of the internal flow; the higher the pressure differences between internal and external flow, the stronger the expansion of the internal flow. These effects can also be observed in the next two planes, in which the differences become even more obvious. In the lower part



**Fig. 14** Pitot-pressure measurements at two different  $Re_U$  and two different  $\Pi$  at four different planes downstream of the nozzle.

of the measurement plane, it can be seen that not only does the position of the shear layer differ markedly between the two conditions, but also that its aforementioned asymmetry can be observed as well. A reason for this, as already discussed, is the asymmetric side injection of the internal gas, streaming slightly from the right to the left in the downstream direction. In the upper part of the measurement plane, the values for the pressure distribution of the two conditions differ due to the different strength of the expansion being influenced by the nozzle pressure ratio.

The main (core) nozzle flow is not influenced by the external flow and does not differ markedly for the two conditions, as can be seen in Figs. 14a and 14b by looking at the high-pressure region. The size and the normalized pressure values of this region do not change for different  $\Pi$ . This verifies that the main core nozzle flow is largely independent of  $\Pi$  and  $Re_U$ .

#### E. Comparison of PSP and Pitot Measurements Results

Figures 15a–15d compare the results obtained by the PSP method and from the pitot-pressure measurements. These figures give an impression of how the two measurement techniques complement each other. The direction of view is downstream (from bottom to top), looking at the expansion ramp and the two measurement planes in each figure. In Figs. 15a and 15c, the entire expansion ramp and the first two measurement planes ( $x = 207$  and  $244$  mm) are depicted, whereas Figs. 15b and 15d show only the end of the expansion ramp and the last two measurement planes ( $x = 274$  and  $304$  mm). Presented are the results at two different nozzle pressure ratios ( $\Pi = 250$  and  $500$ ), all at the same  $Re_U = 8 \times 10^6$ . By comparing in

this way, one can get not only a better phenomenological impression of the nozzle flow for this special case, but one can also summarize all of the preceding phenomena in the one figure. The asymmetry caused by the slightly turned flow direction from the right to the left in the downstream direction can be observed, as can the region of almost no flow on the left side of the expansion ramp. The different size of the region in which the expansion fan impinges on the expansion ramp due to the different  $\Pi$ , causing the static pressure to increase and decrease, can be seen when comparing Figs. 15a and 15c. In this top view, the shock emanating from the right corner of the trailing edge of the cowl can be seen propagating toward the shifted and turned symmetry line and interacting with the reflected expansion fan. This is a good example of two different diagnostic methods, PSP and pitot-pressure measurement, complementing each other to help visualize and understand the complex flow structure generated by the slightly asymmetric flow and the strong interactions between the expansion fan and the reflected shock wave.

The pitot-pressure measurements shown in these figures reveal that there are differences in the upper and lower regions of the measurement planes in which the influence of the external flow depends on  $\Pi$ . The main core flow, however, is independent of  $Re_U$  and  $\Pi$ , as these figures show.

## IV. Conclusions

An experimental study was conducted with a nozzle/afterbody model to characterize the flowfield created by the interaction of a single-expansion-ramp nozzle flow with an external hypersonic flow. For a better understanding of the physical phenomena involved, of the influence of different parameters on the nozzle flow properties and nozzle performance, and of the complex interactions between the internal nozzle and the external flows, the pitot-pressure measurement and the pressure-sensitive-paint (PSP) methods were applied.

The feasibility and potential of the PSP method for such applications was demonstrated. With the help of the PSP results, the flowfield could be visualized and the wavy character of the static pressure distribution, obtained previously with PSI pressure-sensors, could be better understood. The results also revealed that the flowfield is asymmetric, most likely due to the single-hole injection of the nozzle gas through only the one side wall in the forebody. The PSP method also helped in the understanding and interpretation of the complex flow phenomena and the spatially wavy behavior of the pressure distribution that are brought about by the interaction of the expansion fan and the shock wave emanating from the side wall; this is important for designing single-expansion-ramp nozzles and optimizing their thrust-generation efficiency.

The simultaneous use of IR thermography provided the temperature distribution on the surface of the expansion ramp. However, because of the high heat conductivity of the metallic model, detection of the flow patterns by IR thermography was not possible. In future work, therefore, an expansion ramp made of a material with low heat conductivity might enable one to better visualize the flow structure using this technique.

Pitot-pressure measurements provided visualization of the flowfield and were most useful in the identification of flow gradients; they could also be used to estimate the size of the exhaust plume and to get the position of shear layers and shocks. By using them, one gains information about the flow behavior in the wake of the nozzle and the interaction between the internal and external flow. The results show that the main supersonic core nozzle flow is not influenced by the external flow conditions (i.e., neither by  $\Pi$  nor by  $Re_U$ ). The behavior of the shear layer, however, was shown to be influenced by these two parameters.

It is generally known that the flow characteristics strongly depend on the geometry of the single-expansion-ramp nozzle. This makes it important to have a nozzle for which the design pertains as closely as possible to its expected operating range. The internal nozzle flow is largely influenced by the geometry of the nozzle, but the interaction between internal and external flows depends on both the nozzle pressure ratio  $\Pi$  and the freestream Reynolds number. The position

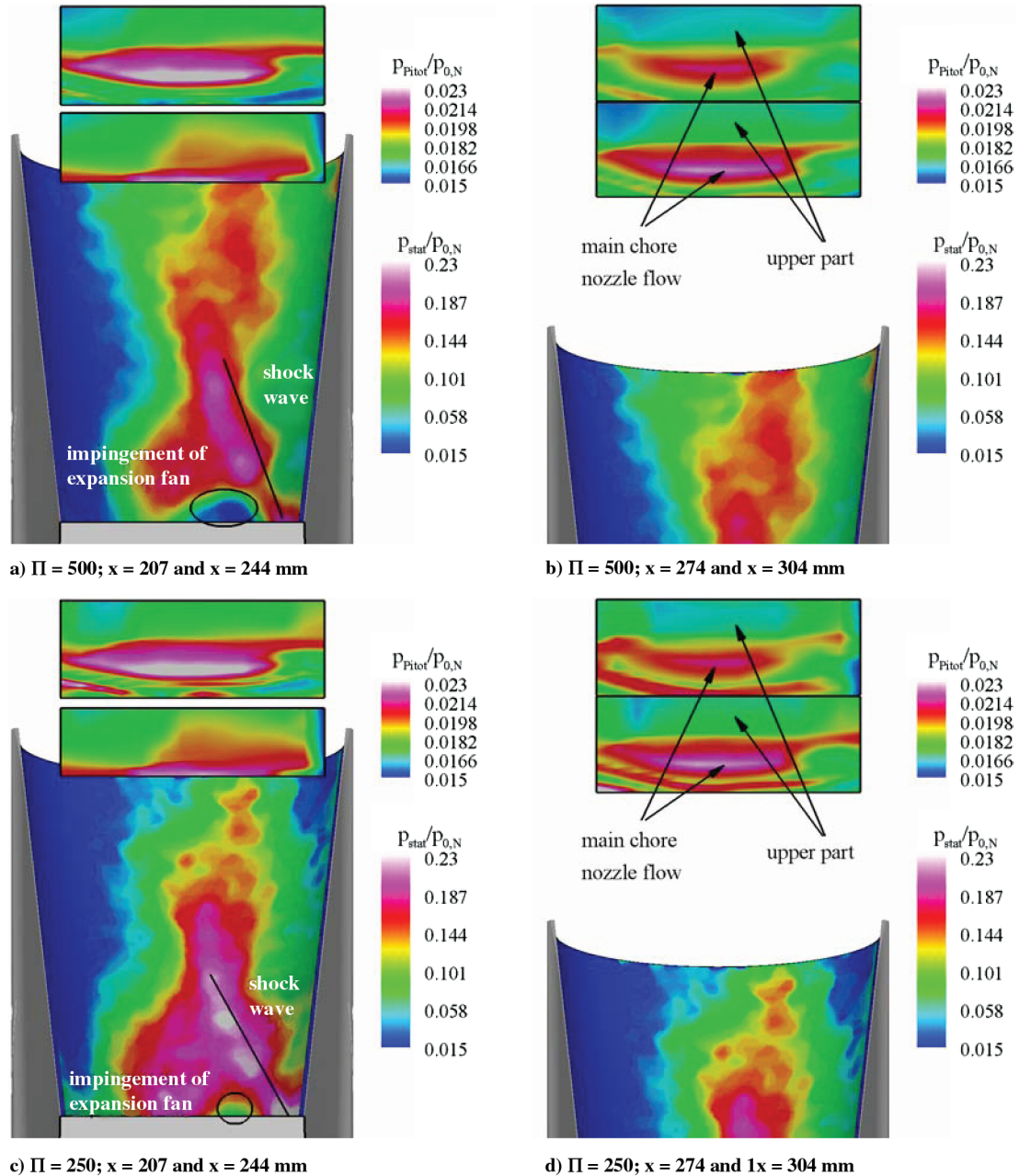


Fig. 15 Comparison between pitot (at all planes) and PSP (on the expansion ramp) pressure measurements at freestream Reynolds numbers  $Re_U = 8 \times 10^6$  and two different nozzle pressure ratios  $\Pi = 250$  and  $500$ .

of the exhaust plume is independent of the flow parameters such as the total nozzle pressure, but is dependent on the geometry of the nozzle. So it can be said that the gross thrust depends mainly on the geometric shape of the nozzle and on  $\Pi$ , but does not depend strongly on  $Re_U$ , at least not within the investigated Reynolds number range here. The total net thrust of the scramjet engine, however, obviously depends on the freestream Reynolds number.

To accomplish a more symmetric nozzle flowfield, a new model with improved gas injection will be tested in the near future.

### Acknowledgments

The financial support for this work by the German National Research Council (DFG) within the Graduate Student Research Group (Graduiertenkolleg) "Aerothermodynamic design of a scramjet propulsion system for future space transportation" and by the DLR, German Aerospace Center is gratefully acknowledged. The authors would especially like to thank the following colleagues in the Institute of Aerodynamics and Flow technology for their

valuable contributions to this work: Ch. Klein, W. Sachs, U. Fey, P. Herzog, M. Janke, D. Lütz, J. Häberle, P. Gruhn.

### References

- [1] Walther, R., "Scramjet-Propulsion: Alte Herausforderung im Neuen Jahrhundert?," *Jahrbuch 2003*, Deutsche Gesellschaft für Luft- und Raumfahrt, Bonn, Germany, 2003, pp. 755–764.
- [2] Curran, E. T., and Murthy, S. N. B., *Scramjet Propulsion*, Progress in Astronautics and Aeronautics, Vol. 189, AIAA, Reston, VA, 2000.
- [3] Fry, R. S., "A Century of Ramjet Propulsion Technology Evolution," *Journal of Propulsion and Power*, Vol. 20, No. 1, 2004, pp. 27–58. doi:10.2514/1.9178
- [4] Spaid, F. W., and Keener, E. R., "Hypersonic Nozzle/Afterbody CFD Code Validation, Part 1: Experimental Measurements," 31st Aerospace Sciences Meeting and Exhibit, Reno, NV, AIAA Paper 93-0607, 1993.
- [5] Spaid, F. W., Keener, E. R., and Hui, F. C. L., "Experimental Results for a Hypersonic Nozzle/Afterbody Flow Field," NASA Ames Research Center, TM-4638, Moffett Field, CA, 1995.
- [6] Gruhn, P., Henckels, A., and Sieberger, G., "Improvement of the SERN Nozzle Performance by Aerodynamic Flap Design," *Aerospace*

- Science and Technology*, Vol. 6, No. 6, 2002, pp. 395–405.  
doi:10.1016/S1270-9638(02)01177-X
- [7] Flandro, G. A., Roach, R. L., and Buschek, H., “Dynamic Interactions Between Hypersonic Vehicle Aerodynamics and Propulsion System Performance,” NASA, CR-190638, 1992.
- [8] Edwards, T. A., “The Effect of Exhaust Plume/Afterbody Interaction on Installed Scramjet Performance,” NASA, TM-101033, 1988.
- [9] Baysal, O., “Flow Analysis and Design Optimization Methods for Nozzle Afterbody of a Hypersonic Vehicle,” NASA, CR-4431, 1991.
- [10] Ebrahimi, H. B., “An Efficient Two-Dimensional Engineering Design Code for Scramjet Combustor, Nozzle, and Plume Analysis,” 29th Aerospace Sciences Meeting, Reno, NV, AIAA Paper 91-0416, 1991.
- [11] Ishiguro, T., Takaki, R., Mitani, T., and Hiraiwa, T., “Three-Dimensional Analysis of Scramjet Nozzle Flows,” AIAA/DGLR Fifth International Aerospace Planes and Hypersonics Technologies Conference, München, AIAA Paper 1993-5059, 1993.
- [12] Tatum, K., Monta, W., Witte, D., and Walters, R., “Analysis of Generic Scramjet External Nozzle Flowfields Employing Simulant Gases,” AIAA Second International Planes Conference, Orlando, FL, AIAA Paper 90-5242, 1990.
- [13] Keener, E. R., “Experimental Research of the Aerodynamics of Nozzles and Plumes at Hypersonic Speeds,” NASA, CR-187316, 1992.
- [14] Carboni, J. D., Shyne, R. J., Leavitt, L. D., Taylor, J. G., and Lamb, M., “Supersonic Investigation of Two Dimensional Hypersonic Exhaust Nozzles,” NASA, TM-105687, 1992.
- [15] Lindblad, I. A. A., Grönland, T. A., Cambier, J.-L., Wallin, S., Behrens, T. M., Sacher, P., and Netterfield, M., “A Study of Hypersonic Afterbody Flowfields,” AIAA Paper 97-2289, 1997.
- [16] Tomioka, S., Hiraiwa, T., and Mitani, T., “A Study on Boundary Layer in a Scramjet Nozzle Operating Under High Enthalpy Conditions,” 30th AIAA/ASME/SAE/ASEE Joint Propulsion Conference, Indianapolis, IN, AIAA Paper 1994-2820, 1994.
- [17] Weigand, B., Gaisbauer, U., Reinhartz, B., Kau, H.-P., and Schröder, W., *Aero-Thermodynamische Auslegung Eines Scramjets: Antriebs-systems für Zukünftige Raumtransportsysteme*, Deutsche Gesellschaft für Luft- und Raumfahrt, Bonn, Germany, 2006.
- [18] Mitani, T., Kanda, T., Hiraiwa, T., Igarashi, Y., and Nakahashi, K., “Drags in Scramjet Engine Testing: Experimental and Computational Fluid Dynamics Studies,” *Journal of Propulsion and Power*, Vol. 15, No. 4, 1999, pp. 578–583.
- [19] Hirschen, C., Gülhan, A., Beck, W. H., and Henne, U., “Experimental Study of the Interaction Between Internal and External Flows of a Scramjet Nozzle Using Various Diagnostic Techniques,” 43rd AIAA/ASME/SAE/ASEE Joint Propulsion Conference and Exhibit, Cincinnati, OH, AIAA Paper 2007-5088, 2007.
- [20] Hubner, J. P., Carroll, B. F., Schanze, K. S., Ji, H. F., and Holden, M. S., “Temperature- and Pressure-Sensitive Paint Measurements in Short-Duration Hypersonic Flow,” *AIAA Journal*, Vol. 39, No. 4, 2001, pp. 654–659.
- [21] Matsumura, S., Schneider, S. P., and Berry, S. A., “Streamwise Vortex Instability and Transition on the Hyper-2000 Scramjet Forebody,” *Journal of Spacecraft and Rockets*, Vol. 42, No. 1, 2005, pp. 78–89.  
doi:10.2514/1.3959
- [22] Hirschen, C., Gruhn, P., and Gülhan, A., “Influence of Heat Capacity Ratio on the Interaction Between External Flow and Nozzle Flow of a Scramjet,” 14th AIAA/AHI International Space Planes and Hypersonic Systems Technologies Conference, Canberra, Australia, AIAA Paper 2006-8095, 2006.
- [23] Novelli, P., and Koschel, W., “JAPHAR: A Joint Onera—DLR Project on High Speed Airbreathing Propulsion,” International Symposium on Air Breathing Engines Paper 99-7091, 1999.
- [24] Klein, C., Engler, R. H., Henne, U., and Sachs, W. E., “Application of Pressure-Sensitive Paint (PSP) for Determination of the Pressure Field and Calculation of Forces and Moments of Models in a Wind Tunnel,” *Experiments in Fluids*, Vol. 39, No. 2, 2005, pp. 475–483.  
doi:10.1007/s00348-005-1010-8
- [25] Liu, T., Guille, M., and Sullivan, J. P., “Accuracy of Pressure-Sensitive Paint,” *AIAA Journal*, Vol. 39, No. 1, 2001, pp. 103–112.
- [26] Sajben, M., “Uncertainty Estimates for Pressure Sensitive Paint Measurements,” *AIAA Journal*, Vol. 31, No. 11, 1993, pp. 2105–2110.
- [27] Klein, C., Niebergall, S., Sachs, W. E., Henne, U., and Engler, R. H., “PSP Measurements on a Linear Plug Nozzle: Aerodynamic Investigation of Linear Plug Nozzle Configurations,” *New Results in Numerical and Experimental Fluid Mechanics IV*, Notes on Numerical Fluid Mechanics and Multidisciplinary Design, Vol. 87, Springer-Verlag, New York, 2004, pp. 260–269.

R. Bowersox  
Associate Editor